



HAL
open science

Chemiluminescence of burner-stabilized premixed laminar flames

Yi Ding, Daniel Durox, Nasser Darabiha, Thierry Schuller

► **To cite this version:**

Yi Ding, Daniel Durox, Nasser Darabiha, Thierry Schuller. Chemiluminescence of burner-stabilized premixed laminar flames. *Combustion Science and Technology*, 2019, 191 (1), pp.18-42. 10.1080/00102202.2018.1558391 . hal-02135729

HAL Id: hal-02135729

<https://hal.science/hal-02135729>

Submitted on 21 May 2019

HAL is a multi-disciplinary open access archive for the deposit and dissemination of scientific research documents, whether they are published or not. The documents may come from teaching and research institutions in France or abroad, or from public or private research centers.

L'archive ouverte pluridisciplinaire **HAL**, est destinée au dépôt et à la diffusion de documents scientifiques de niveau recherche, publiés ou non, émanant des établissements d'enseignement et de recherche français ou étrangers, des laboratoires publics ou privés.




Open Archive Toulouse Archive Ouverte (OATAO)

OATAO is an open access repository that collects the work of some Toulouse researchers and makes it freely available over the web where possible.

This is an author's version published in: <https://oatao.univ-toulouse.fr/23421>

Official URL : <https://doi.org/10.1080/00102202.2018.1558391>

To cite this version :

Ding, Yi and Durox, Daniel and Darabiha, Nasser and Schuller, Thierry 
Chemiluminescence of Burner-Stabilized Premixed Laminar Flames. (2019) *Combustion Science and Technology*, 191 (1). 18-42. ISSN 0010-2202

Any correspondence concerning this service should be sent to the repository administrator:

tech-oatao@listes-diff.inp-toulouse.fr

Chemiluminescence of Burner-Stabilized Premixed Laminar Flames

Y. Ding^{a,b}, D. Durox^a, N. Darabiha^a, and T. Schuller^{a,c}

^aLaboratoire EM2C, CNRS, CentraleSupélec, Université Paris Saclay, Gif-sur-Yvette, France; ^bBosch Thermotechnologie, Stalingrad, Drancy, France; ^cInstitut de Mécanique des Fluides, IMFT, Université de Toulouse, CNRS, Toulouse, France

ABSTRACT

The OH*, CH* and CO₂* chemiluminescence signals of methane/air premixed laminar flames stabilized over a nonadiabatic porous plug burner are compared to the signals measured from a nearly adiabatic conical flame in a series of experiments. The impact of reactant stream temperature is also characterized. A numerical study based on 1-D flame models then follows to support the experimental results. It is found both in experiments and in simulations that the linear relationship between the mixture flowrate and the chemiluminescence intensities is no longer valid when flames are closely attached to the burner surface due to the heat transfer between the flame and the burner. The transition between the linear and the nonlinear regimes is identified as the gas flow velocity drops below the adiabatic laminar burning velocity calculated at the bulk temperature of the flow leaving the burner. When the mass flowrate is kept constant, preheating of the reactant stream increases the chemiluminescence intensity for a freely propagating flame, but has almost no impact for a burner-stabilized flame. It is finally found that the OH* and CH* chemiluminescence intensities correlate with the burnt gas temperature for the adiabatic but also the nonadiabatic flames. The underlying physical mechanisms are discussed. Finally, the evolution of the CH*/OH* ratio with the inlet gas velocity is discussed.

KEYWORDS

Flame chemiluminescence; non adiabatic combustion; preheating; heat losses; operating point control

Introduction

The flame chemiluminescence provides useful information about the combustion process. Considerable progress has been made on the use of the chemiluminescence signal for the monitoring of heat release rate, equivalence ratio, pollutant gas emissions and also sensing thermo-acoustic instabilities (Zimmer et al., 2003; Hardalupas et al., 2004, 2010; Geddis, 2009; Lauer and Sattelmayer, 2010; Lauer et al., 2011; Guethe et al., 2012). There are many examples of the use of the chemiluminescence signal to get an estimate of the state of combustion.

The following examples are a selected number of samples covering different applications. Docquier et al. (2002) developed a demonstrative closed-loop equivalence ratio controller for laminar CH₄/air premixed conical flames up to 20 bar, using the chemiluminescence intensity ratios OH*/CH* and CO₂*/CH*. Monitoring the equivalence ratio on an industrial swirling burner is reported by Guyot et al. (2010). Hardalupas et al. (2010) have shown that OH*, CH* and CO₂* are good indicators for the heat release rate in

a model gas turbine combustor. Arias et al. (2008) used silicon photodiodes with interference optical filters to control a central heating burner and have correlated the CH^*/C_2^* ratio with the CO emission and combustion efficiency.

The chemiluminescence signal depends on the injection flowrate, temperature, pressure, strain rate, fuel composition and many other factors (Ballester et al., 2009, García-Armingol and Ballester, 2014b; Hardalupas and Orain, 2004; Higgins et al., 2001a, 2001b; Nori and Seitzman, 2007, 2009; Orain and Hardalupas, 2010). Consequently when it is used to infer a certain combustion parameter, the impact of all other factors altering this parameter needs to be considered as well. In many combustion devices, it is shown that the chemiluminescence intensity of laminar premixed hydrocarbon/air flames is proportional to the bulk flow velocity when the burner is operated at a fixed equivalence ratio (Hurle et al., 1968 Higgins et al., 2001a, 2001b). Taking the ratio of two chemiluminescence intensities (Kojima et al., 2000 Docquier et al., 2002) is a useful technique to obtain signals independent of the flowrate and strain rate. The experimental work of Hardalupas and Orain (2004) with a counterflow burner revealed that the CH^*/OH^* ratio is barely modified by the strain rate. This conclusion was later verified in the numerical investigation from Panoutsos et al. (2009). They showed that even though the strain rate modifies both OH^* and CH^* emissions, the ratio of the two intensities remains unaltered by the strain rate. They however found that the C_2^*/CH^* ratio is modified by strain rate for rich flames. The impact of fuel composition has also already been addressed in a series of studies (Orain and Hardalupas, 2010; García-Armingol and Ballester, 2014a, 2014b; Guiberti et al., 2017).

In idealized gas turbines, counterflow burners or conical flame burners, combustion can be considered to be roughly adiabatic as the heat transfer with the solid components of the system remains small compared to the heat released by combustion to the flow. This is not the case for flames stabilized by perforated burners used for example in heating equipment as illustrated in Figure 1 (Kedia and Ghoniem, 2012). These burners operate in general with laminar flames and with a large turndown ratio. At low power, the flames are stabilized close to the burner surface with large heat transfer to the burner. This operation mode allows to reduce the flame temperature and mitigate NO_x emissions (de Goey et al., 2011). Another example is the porous radiating burner for which combustion takes place

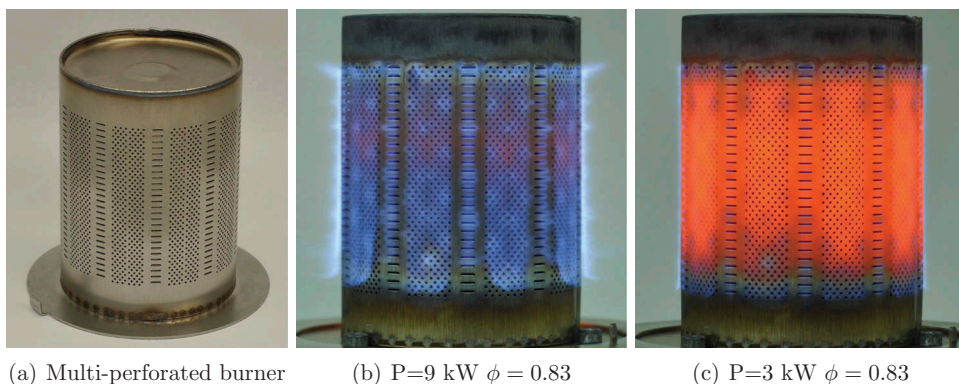


Figure 1. Photos of the cylindrical multi-perforated burner (a), working under regular mode (b) and radiation mode (c).

inside the porous structure and the heat transfer between the flame and this structure generates an excess-enthalpy flame (Barra and Ellzey, 2004; de Goey et al., 2011).

Effects of heat losses on chemiluminescence have to our knowledge not been analyzed in a systematic way. A better knowledge would ease the design of operation point controllers based on sensing the chemiluminescence signal. The main objective of this study is to characterize changes of the flame chemiluminescence properties when heat losses to the burner and preheating have to be considered.

In the present study, the chemiluminescence from flames stabilized on a cylindrical multi-perforated burner is first examined to illustrate effects of heat transfer from the flame to the burner in a practical commercial system. Analysis of effects of heat losses on the chemiluminescence is then carried out with two laminar burners, better suited for parametric studies and modeling. The first one is an axisymmetric burner anchoring a relatively large conical premixed flame. In this case, combustion takes place mainly in an adiabatic mode. The second configuration is a porous plug burner anchoring small flames close to the surface with large heat transfer between the flames and the porous injector. In this case, the reactant stream is also preheated by the hot burner.

A numerical investigation of the chemiluminescence from 1-D laminar flames stabilized by heat transfer above a burner is conducted with the REGATH flow solver developed at EM2C laboratory (Candel et al., 2011). The numerical approach solves the balance equations of mass, momentum and energy for a multispecies flow with detailed transport properties of the gases and the GRI 3.0 mechanism for the chemical reactions. The GRI 3.0 mechanism is here extended to include the excited radicals CH^* and OH^* chemistry. Simulations are compared to experimental data gathered from the porous plug burner and provide a support to analyze the experimental results.

The experimental setup is described in the next section. Test procedures for optical and temperature measurements are then carried out. Experimental results are then presented for the two burners investigated. The 1-D numerical model used in this study is then described. The simulation results and comparisons with measurements are discussed in the final section.

Experimental setup

A commercialized multi-perforated burner widely installed in domestic gas boilers is first used to shed light on effects of heat transfer in a practical system. The burner is made of stainless steel designed to resist high flame temperatures, with a diameter of 70 mm (Figure 1a). The surface of the burner consists of hundreds of tiny circular holes of ≈ 0.8 mm diameter and small rectangular slits. The operational power ranges between 3 and 14 kW. At high power, small blue flames are stabilized away from the perforated grid with reduced heat losses to the burner. This operating mode is designated as “regular” and is illustrated in Figure 1b. At low power, the flames are stabilized close to burner surface with large heat transfer to the metallic components (Figure 1c). The burner turns red due to thermal radiation of the metal at high temperature. In this case, the burner works under the so-called “radiation mode”. There is yet to our knowledge no systematic analysis of the evolution of the chemiluminescence signal between these two operating modes.

This investigation is carried out with two laboratory burners featuring different behaviors with respect to heat losses. The first setup is a porous plug burner, which mimics the

behavior of the commercial burner with strong heat exchanges between the flame and the porous injector. The second setup anchors a nearly adiabatic laminar conical flame, which serves as a reference for the measurements. All flames investigated are obtained with methane–air mixtures at atmospheric pressure.

(1) Porous plug burner (Figure 2):

This burner is a round porous plate of 35 mm diameter and 3 mm thickness, composed of packed bronze grains of 0.2 – 0.3 mm diameter. It is supported by a stainless steel plate and fed by the fuel air mixture with a straight duct below. An external heater can be installed upstream of the burner to investigate effects of gas preheating. An integrated thermocouple measures the gas bulk temperature inside the injection tube. Two tiny metallic fixing lugs are installed to prevent the porous plug from being blown out by the flow. The supporting plate is painted in black to minimize light reflection and avoid interferences with optical measurement devices.

For high gas injection velocities, tiny conical flames are formed above the porous plate as shown in Figure 2c. When the gas velocity drops below the adiabatic laminar burning velocity S_L , the small size of the pores between the bronze grains (of the order of 0.1 mm) eliminates the possibility of flashback. It makes the burner different from those superadiabatic burners described for example by Barra and Ellzey (2004), in which the combustion can take place inside the porous structure. With the present burner, the flame is stabilized at least several tenths of a millimeter above the porous plate with a strong heat transfer to the porous element. In this case, the flame speed is lower than the adiabatic laminar burning velocity S_L and a new equilibrium is achieved with the gas flow velocity u_0 . A 1 D planar flame is then observed as in Figure 2d. In practice, the transition between conical and planar flames is progressive and the two types of flame structures can be simultaneously observed over the porous structure for a certain range of flowrates. This is due to the complex porous structure of sintered bronze, leading to a non uniform gas velocity distribution at the burner outlet.

(2) Laminar conical flame burner (Figure 3):

This burner anchors a conical premixed flame. The fuel air mixture entering the plenum passes first through a perforated plate to homogenize the flow, then through a honeycomb structure helping to laminarize it, a mesh wire grid to prevent flashback and break the residual turbulent vortices before entering a converging nozzle. This nozzle guides the flow at the burner outlet and reduces the boundary layer thickness. The gas mixture leaves the burner with a quasi uniform top hat velocity profile (Durox et al., 1997). A ring stabilizer is added at the top of the nozzle to improve flame stabilization and ease measurements over a large range of powers and equivalence ratios. The ring stabilizer features three slits on the top (Johnson et al., 1998). A tiny annular flame is formed above the slits helping to sustain the central conical flame. The internal diameter

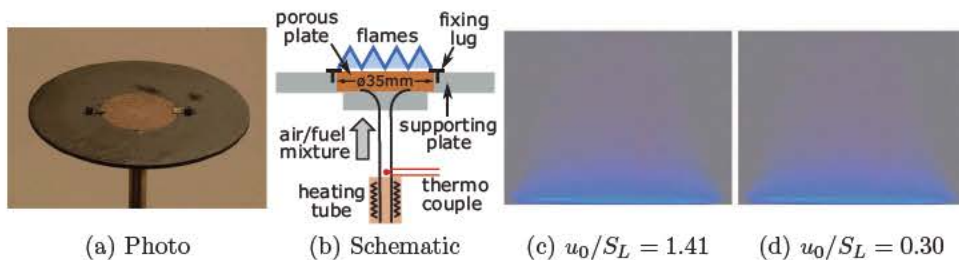


Figure 2. Porous plug burner. u_0 : gas flow velocity at the burner outlet. S_L : adiabatic laminar burning velocity.

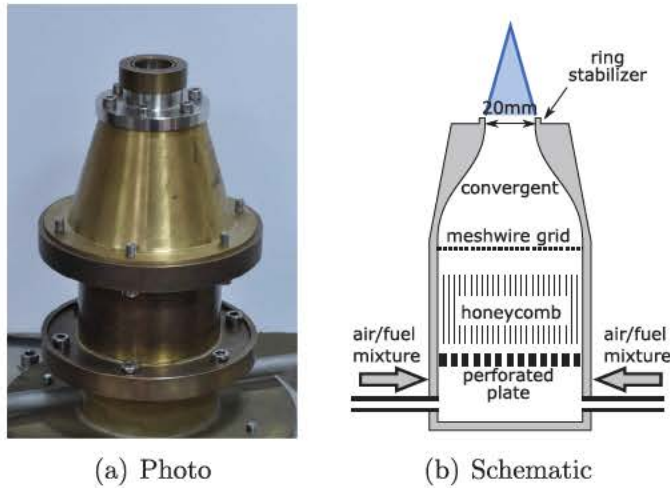


Figure 3. Conical flame burner.

of the ring is 20 mm and corresponds to the diameter of the central conical flame. The height of the central conical flame varies between 40 and 100 mm for the conditions explored. Heat losses from the central flame to the burner are in this case limited because the reaction zone mostly lies far away from the burner, except near the flame base (Mazas et al., 2011; Mejia et al., 2015). The gaseous mixture leaves the burner at nearly room temperature.

Optical measurements

The optical setup is shown in Figure 4. A lens ($F = 10$ mm, $\phi = 3$ mm) collects the light emitted from the flames over a selected region. The light is then guided by an optical fiber to an OceanOptics USB2000+ spectrometer to analyze its spectral content over the range of wavelengths from 200 to 900 nm. The region scrutinized by the spectrometer is a disk of about 100 mm diameter for both burners, which is large enough to collect all the light emitted by the entire combustion region. The conical flame burner (Figure 4a) is observed with a view angle perpendicular to the flow direction. The detector is slightly inclined for the porous plug burner (Figure 4b) measurements to ease light detection because flames are stabilized at a very small distance above the burner surface. In addition to the spectrometer, a Hamamatsu H11902–110 photomultiplier tube mounted with a narrow band bandpass optical filter records the chemiluminescence signal over the entire flame region as shown on the right of the two schematics in Figure 4.

Figure 5 gives an example of spectrum recorded for a stoichiometric conical flame at a power of $P = 2$ kW. One can easily identify the OH^* peak at 308 nm, the CH^* peak at 432 nm and a broadband CO_2^* emission between 300 and 600 nm (Gaydon, 1974). This spectrum does not correspond to the true flame chemiluminescence signal I_0 , but is filtered by the device response function: $I_1 = I_0 R(\lambda)$. The function $R(\lambda)$ has not been characterized because absolute values are not needed for the present study. Only evolutions of the chemiluminescence intensity at fixed wavelengths are examined.

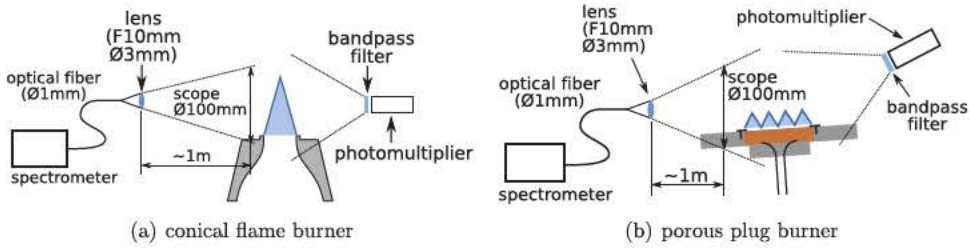


Figure 4. Optical setup for the diagnostics.

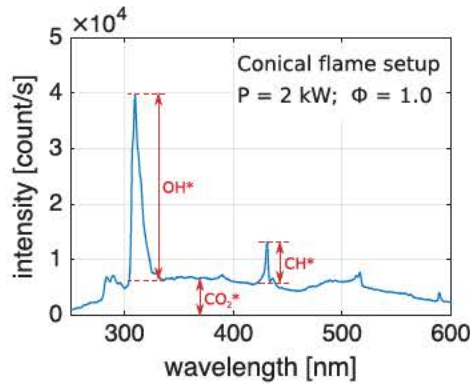


Figure 5. Interpretation of chemiluminescence intensities.

For each burner, CH^* and OH^* emission intensities are deduced from the recorded flame spectra by measuring the height of the emission peaks with respect to the baseline emission background as indicated in Figure 5. This method allows to exclude the CO_2^* broadband emission and stray light. The broadband CO_2^* emission is represented by its intensity value at 370 nm (Samaniego et al., 1995). CO_2^* emission intensities are measured with the photomultiplier tube mounted with a 370 ± 5 nm bandpass filter (see Figure 4), because direct measurements of the CO_2^* signal with the spectrometer have been found to be very sensitive to stray light.

The chemiluminescence intensity is known to be altered by several factors. In the present cases, the flames are laminar and effects of flame curvature (Law, 1989) are limited over the whole surface area of the flames investigated. This approximation is discussed later in the paper when presenting the experimental results in subsection “Specific intensity vs. flowrate”. Moreover, there is no large gradient in the velocity field of the fresh stream of reactants, and effects of strain rate can be ignored. Flames also remain steady in a laminar regime for all the operating conditions investigated. The remaining factors altering the chemiluminescence signal are then the equivalence ratio ϕ , mixture mass flowrate \dot{m} and stream temperature T_0 at the burner outlet. Effects of the equivalence ratio are well known (Hardalupas and Orain, 2004). The main objective of this study is to understand effects of the mixture flowrate (or flame power) and stream temperature on the chemiluminescence signal. Indeed, both can be closely related with burner-flame heat exchange in the investigated configurations.

For adiabatic premixed systems, the chemiluminescence intensity of a given species is found to be proportional to the mixture flowrate (Higgins et al., 2001a, 2001b, Hurlle et al., 1968) when other parameters are kept constant. In this case, the specific intensity remains constant:

$$I_s = I/\dot{m} = cst. \quad (1)$$

where I stands for the measured intensity and \dot{m} the corresponding mixture mass flowrate. In the following, I_s^{exp} designates the measured specific intensities and I_s^{sim} denotes the values found in the simulations.

In a first set of experiments, the proportional relationship Eq. (1) between the chemiluminescence intensity and the mass flowrate injected is assessed for the conical flame burner and for the porous plug burner. In this latter configuration, burner-flame heat exchange takes place and the bulk gas temperature T_0 at the injector outlet could not be kept constant when the mixture mass flowrate \dot{m} was varied. The impact of this temperature increase is ignored in a first step, but an analysis is conducted a posteriori at the end of the subsection ‘‘Specific intensity vs. temperature’’ when presenting the experimental results. Effect of preheating is investigated in a second series of experiments with the porous plug burner. The fuel–air mixture is in this case heated by an electrical heating tube before injection in the burner (see Figure 2b). The experimental conditions explored in this work are summarized in Table 1.

Temperature measurements

The heat flux from the flame to the burner has been investigated by Botha and Spalding (1954) with a water-cooled burner, and more recently by Van Maaren et al. (1994) by measuring the temperature gradient along their porous plug burner. Though heat flux measurements are difficult in the present study, the burner surface temperature is a convenient indicator of the magnitude of the heat flux transferred from the flame to the burner. The evolution of the burner surface temperature is investigated here for the different conditions explored. These measurements are made with a Fluke 572 IR thermometer. The emissivity of bronze is set to be $\epsilon = 0.55$ and the sampling region is a disk of about 20 mm diameter. The radial temperature gradient over the porous plate is not considered here (Van Maaren et al., 1994).

The hot burner also transfers part of the heat to the fresh stream of reactants. Knowledge of the reactant stream temperature is necessary as it may alter the flame chemiluminescence signal. A direct measurement of this temperature is however difficult with the burner in operation. An alternative method is thus used to gain a rough yet reasonable estimation of the gas stream

Table 1. Experimental conditions. The temperature T_u in degrees Celsius denotes the gas temperature at the outlet of the electrical heating tube before the porous plug burner.

No.	Burner	Equivalence ratio	Power [kW]	T_u [°C]
1	Conical flame	0.77 1.00	1.0 2.0	20
2	Porous plug	0.77 1.00	0.6 1.8	20
3	Porous plug	1.00	0.6, 0.8, 1.3, 1.8	20 180

temperature at the injector outlet. The burner is first left working for several minutes until its surface temperature is stabilized. Then the fuel is turned off but the air continues to flow. A thin-type R Pt/Rh thermocouple is immediately approached to the center of burner outlet at a distance of about 1 mm. The bead of the thermocouple is uncoated, but catalytic effects are not expected to be important as the thermocouple is only used to measure the hot air flow temperature after flame is blown off. The response time of the thermocouple is relatively short (of the order of 30 ms) thanks to the small size of the thermocouple bead ($\sim 100 \mu\text{m}$), but setting the thermocouple in place takes about 1 s. The initial instant at which the flame is blown off is denoted as $t = 0$ and the temperature is then recorded over a period of 30 s. An exponential regression of the data and an extrapolation to $t = 0$ are used to infer the inlet gas temperature when the burner is in operation. More details together with a sensitivity analysis to the different errors made with this reconstruction technique are given in Appendix A. This temperature measurement is conducted only at the center of the burner for each operating condition investigated.

Experimental results

Burner and reactant stream temperatures

The porous plug burner surface temperature is plotted in Figure 6a for different operating conditions as a function of u_0/S_L , where u_0 denotes the bulk velocity of the reactant stream at the burner outlet deduced from the mass flowmeter indications and S_L is the adiabatic laminar burning velocity calculated with the REGATH solver later described. Both the flow velocity u_0 and laminar burning velocity S_L are determined for the reactant stream temperature T_0 . For a given mass flowrate, u_0/S_L is a function of the reactant stream temperature T_0 because S_L increases with T_0 faster than u_0 for methane–air mixtures (Konnov, 2015; Lewis and Von Elbe, 1987). Data for T_0 measured at the burner outlet and plotted in Figure 6b are therefore taken into account for the calculation of u_0 and S_L .

In Figure 6a, one notices that the burner surface temperature monotonically decreases for increasing flowrates. Since a higher burner temperature indicates a larger heat flux from the flame to the burner, one may conclude that the heat flux to the burner decreases monotonically for increasing flowrates over the range of conditions investigated ($0.3 < u_0/S_L < 2.5$). The heat transfer from the flame to the burner is strong when

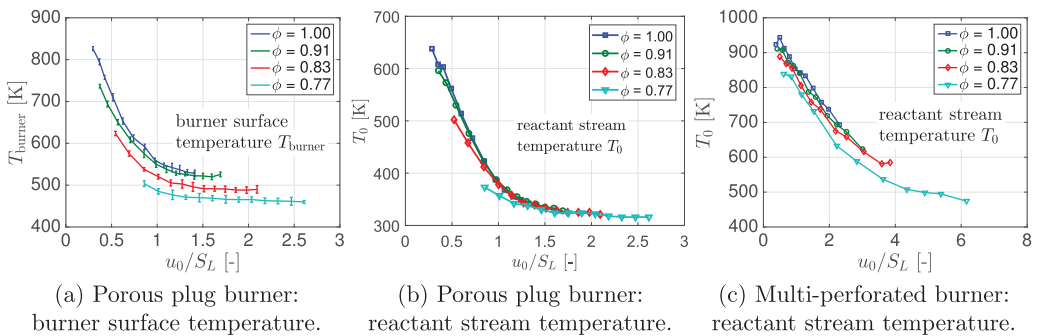


Figure 6. Burner and reactant stream temperature measurements as a function of u_0/S_L . u_0 : gas flow velocity at the burner outlet. S_L : adiabatic laminar burning velocity at T_0 .

$u_0/S_L < 1$. Nevertheless, it is worth pointing out that at very low gas flowrates, the burner temperature drops, and hence the heat lost by the flame as well, due to a lower flame power when the flame is close to blow-off. At high flowrates, the heat transfer between the flame and the burner is less intense, but it does not vanish at least within the investigated range of conditions explored. To confirm these observations, simulations carried out with a 1-D burner-stabilized flame model are compared to heat loss measurements from Botha and Spalding (1954) in the final section of this paper.

The hot burner also transfers part of the energy back to the flame by heating up the reactant stream flowing through the hot sintered bronze. The measured reactant stream temperature at the porous burner outlet is plotted in Figure 6b. It is roughly 200 K below the burner surface temperature.

The reactant stream temperature was also determined on the commercial multi-perforated burner presented in Figure 1 and similar heat exchange phenomena can be identified. The burner temperature is not measured for this burner, but the trend is evidenced by a stronger thermal radiation at low power as illustrated in Figure 1b and 1c. The reactant stream temperature is presented in Figure 6c for different operating conditions. We notice in this case a stronger preheating of the incoming gases compared to the porous plug burner, with a temperature increase of at least 200 K and up to 650 K. This is caused by a higher temperature of the metallic components of the burner and a longer residence time of the gas flow inside the burner.

The multi-perforated commercial burner exhibits thus globally the same thermal behavior as the porous plug burner with (1) a large heat transfer from the flame to the burner inducing (2) a preheating of the reactant stream. The porous plug burner is therefore used in the following to examine effects of heat losses and reactant preheating on the flame chemiluminescence.

Specific intensity vs. flowrate

Conical flame burner

Results are first analyzed for the conical flames stabilized with the setup shown in Figure 3. A series of spectra are recorded for powers ranging within $P = 1.0 - 2.0$ kW and equivalence ratios $\phi = 0.77 - 1.00$. Figure 7 shows for different equivalence ratios the evolution of the specific intensity I_s^{exp} with u_0/S_L and clearly confirms that these quantities are independent. This confirms that the OH^* , CH^* and CO_2^* chemiluminescence intensities linearly increase with the mixture flowrate for adiabatic operating conditions (Higgins et al., 2001a, 2001b, Hurlé et al., 1968).

A brief analysis is made to evaluate the impact of flame stretch on the chemiluminescence signal. The stretch rate for the investigated conical flames hardly exceeds 100 s^{-1} except over a very small fraction of the flame surface at the apex (Law and Sung, 2000). The resulting change of the chemiluminescence intensity is then estimated to be lower than 5% according to the results of Panoutsos et al. (2009). In addition, it can be deduced that for conical flames the stretch rate barely varies with the gas velocity u_0 for a given laminar burning velocity S_L (or equivalence ratio ϕ). Therefore the stretch rate can be considered to remain roughly constant for each curve in Figure 7 and does not modify the shape of the curves.

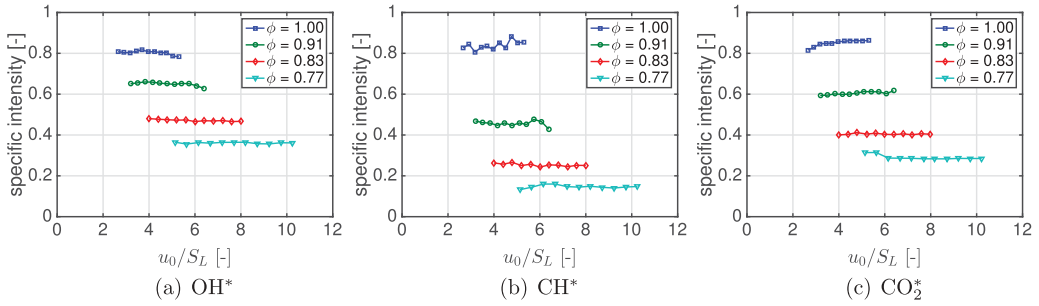


Figure 7. Specific emission intensities I_s^{exp} of OH^* , CH^* and CO_2^* for measurements conducted with the conical flame burner.

Porous plug burner

The same measurements are repeated with the porous plug burner shown in [Figure 2](#) operating at powers $P = 0.6 - 1.8$ kW and equivalence ratios $\phi = 0.77 - 1.00$. Results are presented in [Figure 8](#). We notice here that the behavior of I_s^{exp} may be split into two regimes. The specific intensity remains constant for $u_0/S_L > 1$ and then changes with the mass flowrate injected when u_0/S_L drops below unity. It is here worth reminding that in these figures S_L denotes the adiabatic laminar burning velocity calculated with the REGATH solver for the reactants at the temperature T_0 and u_0 corresponds to the gas flow velocity at the same temperature. The way the bulk temperature T_0 of the reactant stream is determined was described in section “Temperature measurements”.

The left part of the curves plotted in [Figure 8](#) therefore does not obey to Eq. (1) and the proportional relationship between the chemiluminescence intensity and the mixture mass flowrate \dot{m} is violated in this region. It is hypothesized that this phenomenon is due to the heat transfer between the flame and the burner. Heat losses reduce the flame temperature; hence, the specific intensity I_s^{exp} is lower than the value expected for an adiabatic freely propagating flame. When $u_0/S_L > 1$, conical flames are formed above the porous burner, and lie in average further away from the burner surface. In this regime, the combustion reaction mainly takes place at a distance of a few millimeters away from the porous surface. In this case, heat losses to the burner are drastically reduced. The difference between the planar ($u_0/S_L < 1$) and conical flame ($u_0/S_L > 1$) regimes is highlighted in [Figure 2c](#) and [d](#).

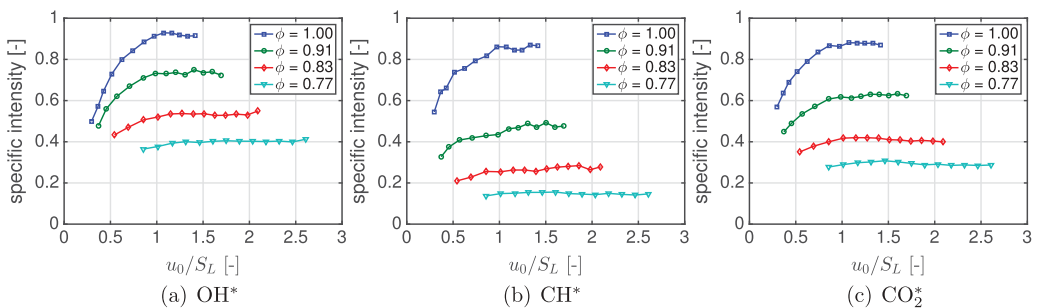


Figure 8. Specific emission intensities I_s^{exp} of OH^* , CH^* and CO_2^* for measurements conducted with the porous plug burner.

These results obtained with the porous plug burner complete those found for the conical flame burner shown in Figure 7. The range of conditions explored in Figure 7 corresponds to $u_0/S_L > 1$, over which I_s^{exp} remains constant. Flames cannot be stabilized above this burner when $u_0/S_L < 1$ due to flashback. Results for the commercial burner shown in Figure 1 are presented in Appendix B. They share the same features as those shown for the porous plug burner in Figure 8.

Specific intensity vs. temperature

The evolution of the chemiluminescence intensity with the bulk stream temperature T_0 is now investigated with the porous plug burner. The reactant stream is preheated by the heating tube at different temperatures from 20°C to 180°C (see Figure 2b) and is then further heated up when flowing through the hot porous plate from the burner. The temperature T_0 of the gaseous stream at the burner outlet is measured with the method described in section “Temperature measurements”. The power ranges between 0.6 and 1.8 kW and the equivalence ratio is set to $\phi = 1.00$.

The specific chemiluminescence intensity is plotted in Figure 9 as a function of T_0 for different values of the mass flux injected. The corresponding values for u_0/S_L are indicated in Figure 9a at the limits of each data set and are the same for the two other graphs. One first notices that for the mass burning flux $f_0 = 6.81 \times 10^{-2} \text{ g cm}^{-2} \text{ s}^{-1}$, the data in blue lie in the regime $u_0/S_L > 1$, corresponding hence to freely propagating flames. In this case, the OH*, CH* and CO₂* chemiluminescence intensities all increase with the reactant stream temperature T_0 . Second, for $f_0 = 3.79 \times 10^{-2}, 3.05 \times 10^{-2}$ and $2.27 \times 10^{-2} \text{ g cm}^{-2} \text{ s}^{-1}$, u_0/S_L is way below unity. These data sets correspond thus to planar flames attached to the burner. In this case, the OH*, CH* and CO₂* chemiluminescence intensities are found to be independent of T_0 , at least over the temperature range investigated. Results obtained for $f_0 = 4.92 \times 10^{-2} \text{ g cm}^{-2} \text{ s}^{-1}$ lie in the regime $u_0/S_L \leq 1$ but are very close to the limit. Due to the nonuniform velocity distribution at the porous plug burner outlet, u_0 can locally exceed S_L even though the average speed still remains below S_L and a fraction of the reaction layer detaches and takes a corrugated shape, while another fraction remains planar and attached to the burner. In this case, the OH*, CH* and CO₂* chemiluminescence intensities slightly increase with T_0 but with a reduced slope. An

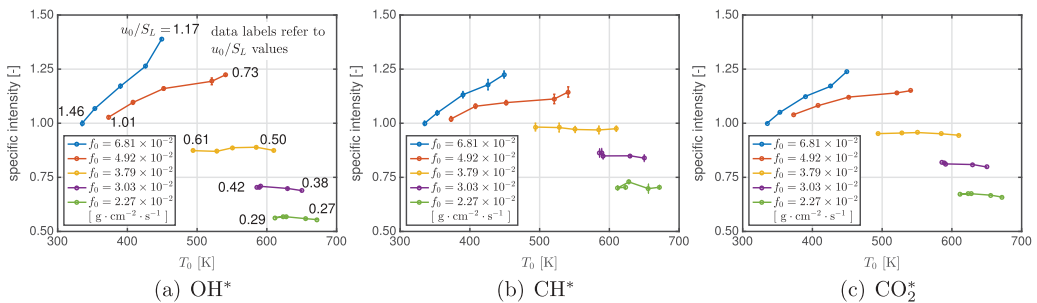


Figure 9. Evolution of the chemiluminescence intensity with the reactant stream temperature T_0 measured on the porous plug burner for stoichiometric mixtures $\phi = 1.00$. The corresponding values for u_0/S_L are indicated at the two ends of each data set gathered at a fixed burning flux f_0 in the left plot. These limits are the same for the two other plots.

interpretation of the behaviors of the free and attached flames is given with the help of the simulation results in the last section of this paper.

It is also worth pointing out that the set of data in blue in Figure 9, though obtained for a fixed mass burning flux of $f_0 = 6.81 \times 10^{-2} \text{g cm}^{-2} \text{s}^{-1}$, is indeed the same for any adiabatic flame with $u_0/S_L \geq 1$, because the specific intensities have been found to be independent of the mixture mass flowrate \dot{m} (or mass burning flux f_0) in this regime. This is highlighted by the first point of the red data set obtained for $f_0 = 4.92 \times 10^{-2} \text{g cm}^{-2} \text{s}^{-1}$ and $u_0/S_L = 1.01$ which lies close to the blue data set obtained for $f_0 = 6.81 \times 10^{-2} \text{g cm}^{-2} \text{s}^{-1}$ in each plot.

Effects of preheating were so far ignored when studying the influence of the mass flowrate injected in the system on the flame chemiluminescence intensities. A discussion of this issue is now conducted. It has been shown that for burner-stabilized planar flames, the temperature T_0 has no effect on the chemiluminescence intensity in Figure 9 when $u_0/S_L \leq 0.6$. For $u_0/S_L > 1$, the chemiluminescence intensity is altered by T_0 , but Figure 6b also reveals that changes of T_0 are relatively small in this regime, and as a consequence they barely alter the measured signal. However, when $0.6 \leq u_0/S_L \leq 1$, the flames are stabilized over the porous plug burner in a complex fashion with a corrugated pattern exhibiting conical and planar shapes. In this regime, variations of T_0 with the flowrate cannot be neglected. As a consequence, the specific intensity plotted in Figure 8 also includes the contribution of T_0 , which moves the experimental points a bit upstream for $0.6 \leq u_0/S_L \leq 1$ and leaves unchanged intensity values for $u_0/S_L \leq 0.6$ and $u_0/S_L > 1$.

Numerical simulations

A numerical analysis is conducted as a support for the experimental findings. Simulations are carried out with the 1-D REGATH flow solver developed at EM2C laboratory. This code includes detailed thermochemical and transport properties and takes into account detailed chemistry (Candel et al., 2011). The GRI 3.0 (Smith et al., 2000) mechanism, including 53 species and 325 elementary reactions, is augmented with OH^{*}- and CH^{*}-related reactions (Alviso et al., 2015; Smith et al., 2002). This augmented mechanism includes the OH^{*} and CH^{*} formation reactions ($\text{CH} + \text{O}_2 \rightarrow \text{OH}^* + \text{CO}$, $\text{O} + \text{H} + \text{M} \rightarrow \text{OH}^* + \text{M}$, $\text{C}_2\text{H} + \text{O} \rightarrow \text{CH}^* + \text{CO}$, $\text{C} + \text{H} + \text{M} \rightarrow \text{CH}^* + \text{M}$), the OH^{*} and CH^{*} radiative decay reactions and the quenching reactions due to the most abundant molecules in the system (N_2 , O_2 , H_2O , H_2 , CO , CO_2 , CH_4). The CO_2^* emission intensity is not taken into account in this numerical analysis.

Two types of flame models are considered: a freely propagating adiabatic model ($u_0/S_L = 1$) and a burner-stabilized non-adiabatic model ($u_0/S_L \leq 1$). The analysis is mainly done with the second model. It considers a semi-infinite region from $x = 0$ to $+\infty$. The presence of the burner is simulated by imposing the following boundary conditions for the k -th species mass fraction Y_k and temperature T of the gases at $x = 0$ (Smooke, 1982):

$$Y_k|_{x=0} + \frac{\rho Y_k V_k}{f_0}|_{x=0} = Y_k^0 \quad (2)$$

$$(\rho u)|_{x=0} = f_0 \quad (3)$$

$$T|_{x=0} = T_0 \quad (4)$$

where V_k is the species diffusion velocity, ρ the mixture density and f_0 the mass burning flux. The subscript 0 stands for the injection conditions for the stream of reactants at $x = 0$. The heat flux q toward the burner is given by $q = k(\partial T/\partial x)|_{x=0}$, where k is the mixture thermal conductivity. The heat loss q corresponds to a decrease in enthalpy at $x = 0$ and the new gas inlet enthalpy is given by $h'_0 = h_0 - q/(\rho_0 u_0)$.

In this numerical model it is assumed that the heat exchanges between the gaseous mixture within the burner and the metallic components of the burner are fast enough to reach the chemical and thermal equilibrium at the burner outlet corresponding to the numerical domain inlet at $x = 0$. Heat transfer by radiation is weak compared to heat conduction and is neglected in this study.

In Eq. (3), f_0 is assigned to different values to account for the change of gas flowrate. For a 1-D flame model, solutions exist only for $u_0 = f_0/\rho_0 \leq S_L$. When $u_0 = S_L$ the obtained solution is a freely propagating flame under adiabatic conditions. For $u_0 < S_L$ the solution corresponds to a flame attached to the burner stabilized by heat loss. Typical profiles of temperature and species concentrations calculated with the REGATH code are shown in Figure 10. The bulk gas temperature can be varied in the model by changing the value of T_0 in Eq. (4).

The chemiluminescence intensity is determined by the concentration of excited radicals. However, all excited radicals do not emit a photon. Instead, most of them end up with a collisional quenching without light radiation. The method described by Kojima et al. (2005) is therefore used to take into account the fluorescence yield y_i , i.e. the fraction of radiative decay of the i -th excited radical. The chemiluminescence intensity profile $I_i(x)$ of the i -th excited species (OH^* or CH^*) can be written as $I_i(x) = y_i c_i^*$ where c_i^* is the concentration of the i -th excited species. The fluorescence yield y_i is given by $y_i = A_{21}/(A_{21} + Q_{21})$ where A_{21} denotes the rate of radiative decay and Q_{21} the global rate of quenching, calculated by

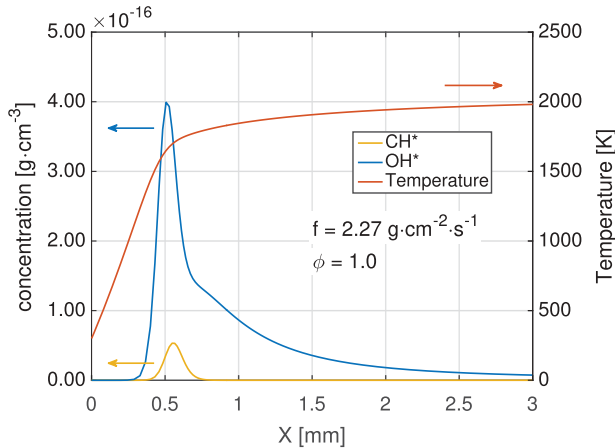


Figure 10. Typical temperature, OH^* and CH^* concentration profiles for a burner-stabilized flame with $u_0/S_L < 1$. $x = 0$ mm corresponds to the burner outlet.

$Q_{21} = \sum_j c_j k_j$, with c_j the concentration of the j -th perturbing molecule (N_2 , O_2 , H_2O , H_2 , CO , CO_2 , CH_4) and k_j the corresponding quenching reaction rate. The quantities A_{21} and k_j can be found in the chemical reaction mechanism (see Smith et al. (2002); Alviso et al. (2015)).

An integration of the emission intensity profiles I_i over the numerical domain gives the chemiluminescence intensity of a unit flame surface area. The specific intensity is then calculated as:

$$I_{s,i}^{sim} = \frac{\int_0^L I_i dx}{f_0} \quad (5)$$

The size of the numerical domain L is chosen to be 1 cm, including the flame front and the hot region of burnt gases of the simulated flames.

Numerical results and validations by experiments

Temperature profile

Figure 11 shows a zoom on temperature profiles over $x = 0. - 0.8$ mm for stoichiometric mixtures injected at $T_0 = 298$ K with three different mass burning fluxes $f_0 = 4.36 \times 10^{-2}$, 4.00×10^{-2} and $3.50 \times 10^{-2} \text{ g cm}^{-2} \text{ s}^{-1}$. It is reminded that the temperature at $x = 0.8$ mm is not the equilibrium burnt gas temperature T_b as the reaction is not complete at this point. The mass flux $f_0 = 4.36 \times 10^{-2} \text{ g cm}^{-2} \text{ s}^{-1}$, corresponding to an inlet velocity of $u_0 = 38.7 \text{ cm s}^{-1}$, is the maximum value yielding a solution to the problem, and corresponds therefore to an adiabatic freely propagating flame. In this case, the temperature and all species gradient vanish at $x = 0$. The other solutions obtained for lower mass burning fluxes f_0 are stabilized by the flame-burner heat exchange. They feature a positive temperature gradient at $x = 0$, revealing a finite heat flux q toward the burner inlet.

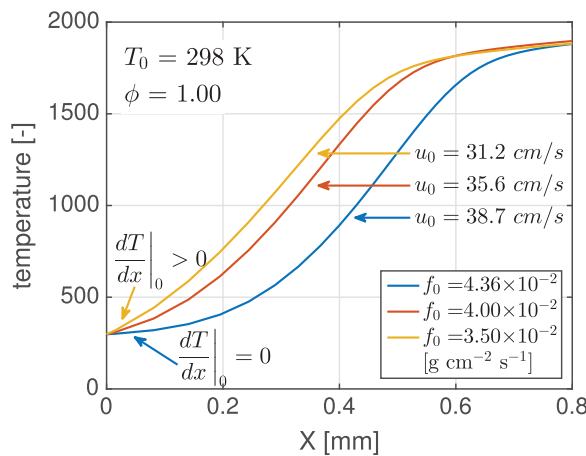


Figure 11. Temperature profiles calculated for different flowrates. The temperature at $x = 0.8$ mm should not be confused with the equilibrium temperature T_b of the burnt gases as the reaction is not complete at this point.

Figure 12 shows the evolution of the burnt gas temperature T_b and the fraction ξ_{loss} of heat which is lost with respect to the thermal power as a function of the normalized gas velocity u_0/S_L . The heat loss fraction is calculated as:

$$\xi_{\text{loss}} = \frac{k \frac{dT}{dx} \big|_{x=0}}{\Delta h_{\text{CH}_4}^0 f_0 Y_{\text{CH}_4}} \quad (6)$$

where $\Delta h_{\text{CH}_4}^0$ is the reaction enthalpy per unit mass and Y_{CH_4} the mass fraction of methane. When the gas velocity decreases, the heat losses increase and the burnt gas temperature drops in Figure 12. The simulated behavior of the burner reproduces well the experimental results from Botha and Spalding (1954) obtained for stoichiometric propane-air flames stabilized over a porous plug burner. This behavior is also consistent with the conclusions from the experimental investigation conducted in the previous section except that ξ_{loss} goes to zero at $u_0/S_L = 1$ in Figure 12, while the temperature measurements shown in Figure 6a indicate that heat exchange still persists for $u_0/S_L > 1$ though it is reduced. It is suggested that the difference results from a small fraction of the flame with u_0/S_L locally below unity in the experiments as shown in Figure 2c. This part of the flame also helps to anchor the conical flames above the burner.

Specific intensity vs. flowrate

Simulation results of the specific chemiluminescence intensity given by Eq. (5) for the 1-D burner stabilized flames are displayed in Figure 13 together with the experimental data for the porous plug burner. The reactants are injected in the numerical domain at the same velocity u_0 and temperature T_0 as for the experiments (Figure 6b). To ease comparisons, the scales for the specific intensities I_s^{exp} and I_s^{sim} are adapted so that the values for $u_0/S_L = 1.0$ and $\phi = 1.0$ are set equal to unity.

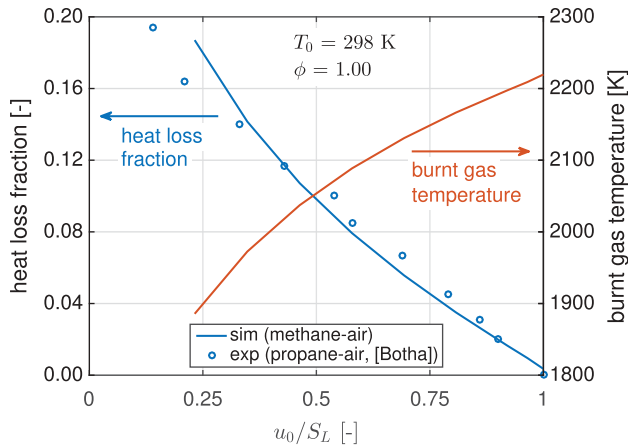


Figure 12. Evolution of the heat loss fraction ξ_{loss} and burnt gas temperature T_b with the normalized flowrate u_0/S_L . The solid lines correspond to simulation results. Circles are experimental results taken from Botha and Spalding (1954).

The simulations support the experimental finding that the specific intensity is not constant in the regime $u_0/S_L < 1$. For CH* (Figure 13b), the simulations (solid lines) match well the experiments (circles). The small difference for $\phi = 0.91$ (dark green) near $u_0/S_L = 1$ can be attributed to a slight drift of the transition point from the linear to the nonlinear regime that can be seen in Figure 8b. This drift causes I_s^{exp} to be slightly underestimated at $u_0/S_L = 1$. For OH* (Figure 13a), the specific intensity values at $u_0/S_L = 1$ are correctly predicted. For $u_0/S_L < 1$, the slope of the curves is relatively well reproduced, but the experimental data lie slightly above the simulation curves. Several explanations are possible: (1) This gap may be due to the omission of the temperature effect in the analysis of the experimental results presented in the previous section and according to the discussion made at the end of this former section, the experimental values are slightly moved upwards. This hypothesis is supported by the fact that the experimental data match again the simulation curve for $u_0/S_L \approx 0.4$ for a stoichiometric mixture in Figure 13a. According to the discussion made on effects of temperature, the impact of preheating should vanish around $u_0/S_L = 0.6$, but it is seen to vanish in Figure 13a for $u_0/S_L = 0.4$. (2) The non-uniformity of the gas velocity distribution at the porous plug burner outlet may also contribute to higher I_s^{exp} values. But this hypothesis does not explain why the CH* intensity is not impacted in Figure 13b. (3) The size of the numerical domain over which the OH* and CH* emission intensities are calculated may also slightly differ from the size of the domain over which the OH* and CH* signals are collected in the experiments. The CH* only being abundant close to the flame front, this signal is not altered by the size over which the integration is performed. The OH* signal however persists in the burnt gases over a larger distance to the flame front and the total OH* emission is thus more sensitive to the extension of the numerical domain.

Specific intensity vs. temperature

The OH*- and CH*-specific intensities calculated by the numerical model are plotted in Figure 14 as a function of the bulk gas temperature T_0 , together with the experimental results (circles with error bars). The scales are adapted with the experimental and

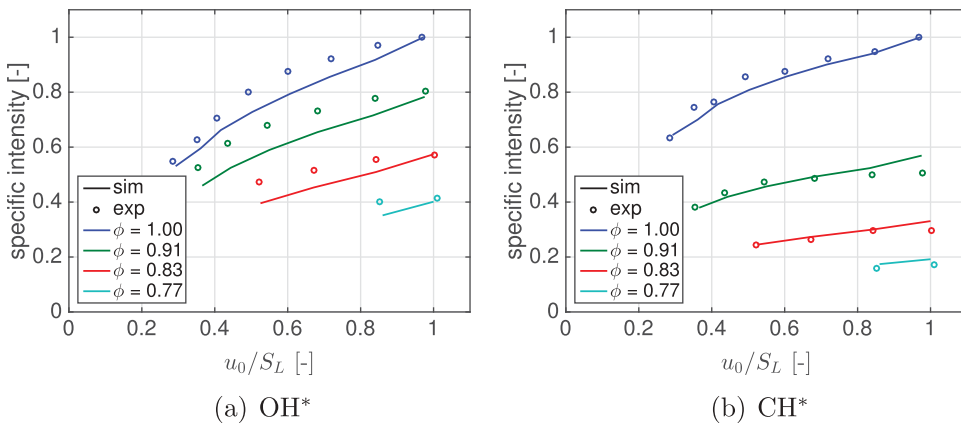


Figure 13. Evolution of OH*- and CH*-specific intensities for the porous plug burner with the normalized gas velocity u_0/S_L at different equivalence ratios. Lines: simulations. Circles: measurements.

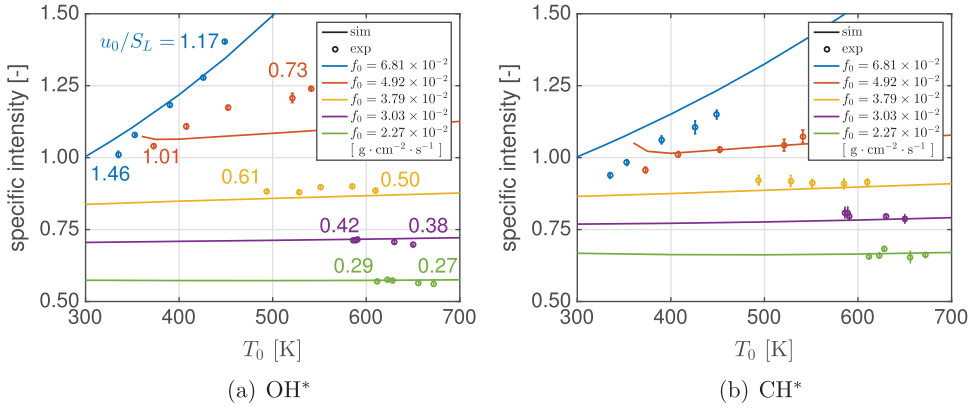


Figure 14. Evolution of OH* and CH* chemiluminescence intensities for stoichiometric mixtures $\phi = 1.00$ and the porous plug burner with the reactant stream temperature T_0 . Lines: simulations. Circles: measurements. Scales are adapted with the experimental and simulation results for the reference mass burning flux $f_0 = 2.27 \times 10^{-2} \text{ g cm}^{-2} \text{ s}^{-1}$.

simulation values for $f_0 = 2.27 \times 10^{-2} \text{ g cm}^{-2} \text{ s}^{-1}$ which serves as a reference. The blue curves in Figure 14a and b for $u_0/S_L = 1$ are calculated with the freely propagating flame model. As explained above, these numerical results are valid for any flame with $u_0/S_L \geq 1$. The other curves are simulated with the burner-stabilized nonadiabatic flame model when $u_0/S_L < 1$.

In both experiments and simulations, the specific intensity increases with T_0 for $u_0/S_L \geq 1$, while for $u_0/S_L < 1$, the specific intensity remains quasi-constant, with a relative variation of less than 5% over the range $T_0 = 300 - 700 \text{ K}$. Simulations reproduce well the experiments for the OH* and CH* signals in most cases. One difference between experiments and simulations concerns results for $f_0 = 4.92 \times 10^{-2} \text{ g cm}^{-2} \text{ s}^{-1}$ where the slope of the numerical predictions for OH* is smaller than the one found in the measurements. This is attributed to the nonuniformity of the gas velocity distribution at the burner outlet in the experiments, a feature which is not considered in the numerical model.

Discussion

The above experiments and simulations reveal that the specific chemiluminescence intensity I_s is altered by the normalized bulk velocity u_0/S_L and the reactant stream temperature T_0 at the injector outlet. A unique rule is proposed here to unify the different results presented above by making use of simulations.

The OH*- and CH*-specific intensities are plotted in Figure 15 as a function of the burnt gas temperature T_b . For each data series, either u_0/S_L or T_0 is kept constant and the other quantity varies. The numerical data calculated for the different operating conditions explored all collapse on a unique curve, highlighting thus a correlation between the burnt gas temperature T_b and the specific intensity I_s^{sim} . This observation also indicates that heat losses alter the chemiluminescence intensity mainly through a change of the burnt gas temperature, probably because most reactions, including the chemiluminescence-related ones, take place at high temperatures close to T_b .

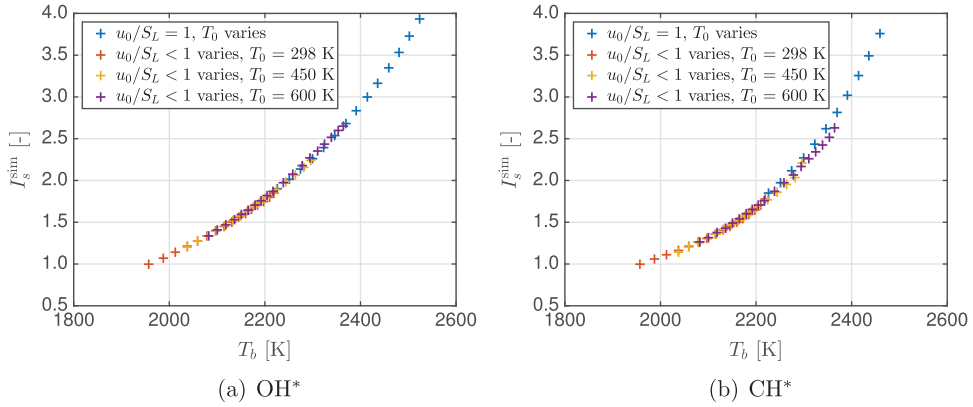


Figure 15. Evolution of the specific intensity I_s^{sim} with the burnt gas temperature T_b calculated by the REGATH solver.

The influence of the inlet gas temperature T_0 for operation at a fixed mass burning flux f_0 is not directly visible in **Figure 15**. It is now demonstrated that the same correlation is also valid in this case. The evolution of T_b with T_0 is presented in **Figure 16** for $u_0/S_L = 1$ and various mass burning fluxes f_0 in the regime $u_0/S_L < 1$. When $u_0/S_L < 1$, the burnt gas temperature T_b is barely altered by changes of T_0 . Changes of T_b are two orders of magnitude lower than the temperature differences for T_0 . Therefore each curve in **Figures 14** and **16** becomes a single point in **Figure 15**.

The quasi-constant temperature T_b observed in the simulations for $u_0/S_L < 1$ in **Figure 16** is due to the fact that there is no significant change of the total enthalpy in the system for the different cases explored. When the reactant stream temperature T_0 at the burner outlet increases, the chemical reactions start earlier and bring the flame closer to the porous wall. It is found in the simulations that the heat loss also increases in this case, and

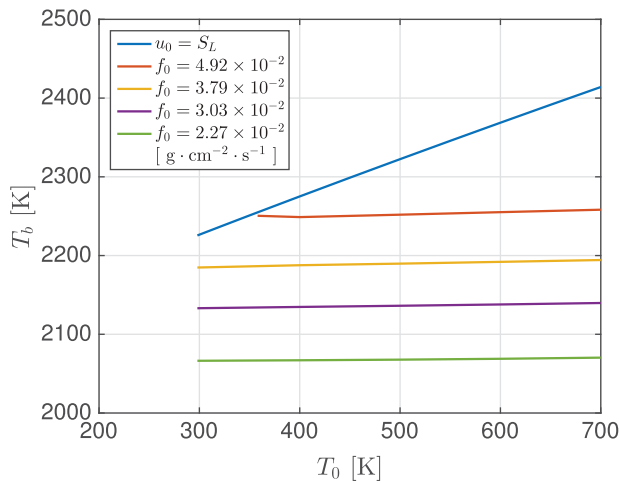


Figure 16. Evolution of the burnt gas temperature T_b with the reactant stream temperature T_0 calculated by the REGATH solver.

approximately equals the excess enthalpy of the reactant stream flowing out of the burner at a higher temperature T_0 . This balance explains why the burnt gas temperature T_b remains almost unchanged. This observation is also supported by asymptotic models of burner-stabilized flames (Borghi and Champion, 2000).

This balance can be understood by examining the boundary conditions Eqs. (2)–(4) of the numerical flame model. The mass burning flux ρu remains constant over the whole numerical domain. In the preheating zone, the mass flowrate of each species remains also constant and $Y_k + (\rho Y_k V_k / \rho_0 u_0)$ remains roughly constant before the chemical reactions take place in the reaction zone (roughly before $T = 1400$ K). Numerical solutions for the temperature and species mass fraction profiles for increasing values of the inlet temperature T_0 correspond to solutions deduced through a translation of an existing solution as long as the inlet boundary condition $x = 0$ still remains in the preheating zone where no chemical reaction takes place. As the temperature gradient vanishes at $x = +\infty$, the burnt gas temperature T_b remains unchanged by this translation. An illustration of this process for the temperature T and CH^* mass fraction profiles is given in Figure 17 for different inlet temperatures T_0 and a fixed mass burning flux $f_0 = 3.79 \times 10^{-2} \text{ g cm}^{-2} \text{ s}^{-1}$. Figure 17 clearly reveals that a translation of the temperature profile to the left leads to larger values of the temperature gradient dT/dx at $x = 0$, and hence also to a larger heat flux from the flame to the burner.

Analysis of the CH^*/OH^* evolution

In many adiabatic systems, the CH^*/OH^* intensity ratio is used as an equivalence ratio indicator, which helps to remove the impact of the flowrate (Docquier et al., 2002; Kojima et al., 2000). It is worth exploring if this intensity ratio is still useful for flame stabilized by heat losses.

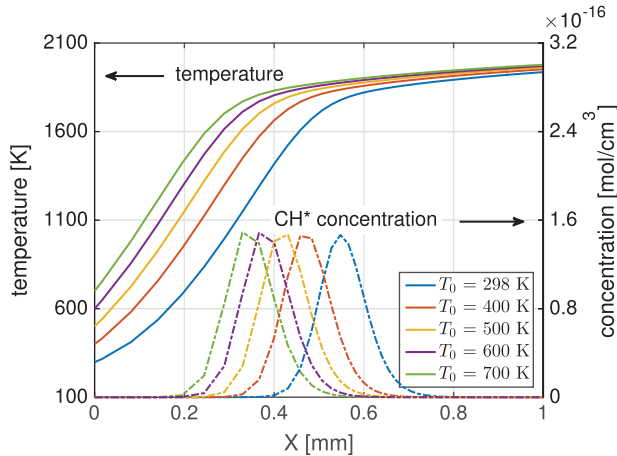
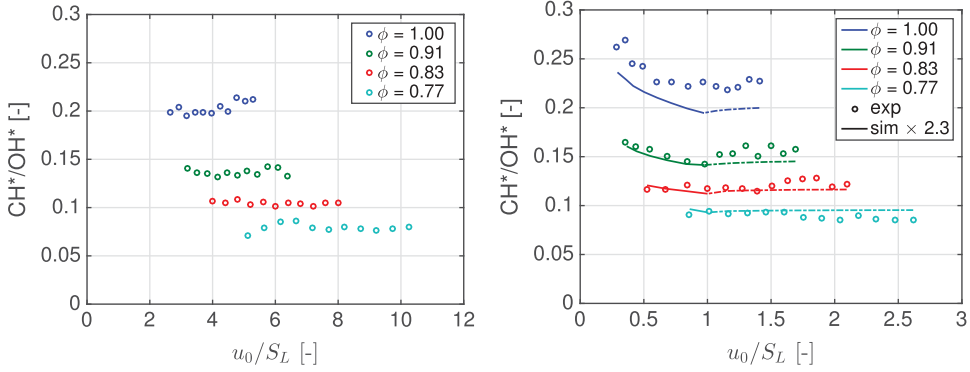


Figure 17. Temperature and CH^* concentration profiles for $T_0 = 298 - 700$ K and $f_0 = 3.79 \times 10^{-2} \text{ g cm}^{-2} \text{ s}^{-1}$.



(a) Experiments gathered on the conical flame burner.

(b) Experiments (circles) gathered on the porous plug burner and numerical simulations (lines).

Figure 18. Evolutions of the CH*/OH* intensity ratios.

The CH*/OH* ratio values obtained from the experiments made with the two burners and the simulations are presented in Figure 18. For the conical flame burner, the CH*/OH* values in Figure 18a are found to be independent of the normalized injection velocity u_0/S_L . As already discussed, heat transfer to the burner remains weak in this configuration and the burner operates mainly in an adiabatic mode. For the porous plug burner, CH*/OH* values (circles in Figure 18b) remain approximately constant in the $u_0/S_L > 1$ regime. In the other regime $u_0/S_L < 1$, values for the CH*/OH* intensity ratio slightly increase when u_0/S_L is reduced, especially for the equivalence ratios $\phi = 0.91$ and 1.00.

An increase of the CH*/OH* ratio at low flowrates when $u_0/S_L < 1$ would cause a small bias error for the equivalence ratio determination. Considering the slope of the CH*/OH* intensity ratio as the equivalence ratio ϕ is varied (Ding et al., 2017), the error is about $\Delta\phi = 0.05$ at $u_0/S_L = 0.3$, and gradually decreases when u_0/S_L approaches unity.

Below $u_0/S_L = 1$, the same trend for the intensity ratio CH*/OH* is supported by the simulations in Figure 18. The numerical results here are multiplied by a factor of 2.3 to take into account the response function of the spectrometer. The curves are calculated with the burner-stabilized flame model for $u_0/S_L < 1$ (solid lines) and the 1-D freely propagating flame model for $u_0/S_L > 1$ (dashed-dotted lines). One may further conclude that the GRI 3.0 mechanism augmented with OH* and CH* reactions well reproduces the evolutions of the CH*/OH* intensity ratio from planar premixed methane air flames stabilized by heat losses. These simulations may in turn be used to ease the development of operating point controllers based on sensing the equivalence ratio for the design of new domestic boilers.

Conclusion

The chemiluminescence of OH*, CH* and CO₂* radicals of laminar methane–air flames has been studied with two burner configurations and a 1-D numerical model. Experimental results provide clear evidences of a nonlinear relationship between the

chemiluminescence intensity signal and the mixture flowrate when the gas injection velocity u_0 drops below the adiabatic laminar burning velocity S_L calculated at the bulk temperature T_0 of the reactant stream at the burner outlet. In this regime, significant heat transfer takes place between the flame and the burner. This conclusion is also supported by simulations of 1-D burner-stabilized flames indicating that the specific intensity of OH^* and CH^* increases with the bulk flow velocity until $u_0/S_L = 1$.

Analysis of effects of the inlet gas temperature has revealed that for a given mass flowrate, the chemiluminescence intensity increases with the inlet gas temperature when $u_0/S_L > 1$, but is barely changed when $u_0/S_L < 1$. The reason is that for the second case, a higher inlet gas temperature causes a stronger heat loss to the burner and the inlet gas enthalpy remains almost unchanged in this balance.

To unify the different findings, a correlation has been introduced between the specific chemiluminescence intensity and the burnt gas temperature that has been revealed with simulations. This correlation has been found to be valid for both burner-stabilized and freely propagating flames and for the different reactant stream temperatures explored.

It has then been shown that the evolution of the intensity ratio CH^*/OH^* is well reproduced by the numerical model with the GRI 3.0 mechanism augmented with reaction mechanisms for OH^* and CH^* species. These simulations may be used in turn to estimate changes of the chemiluminescence signal when heat transfer to the burner needs to be considered.

Nomenclature

λ	Wavelength
ϕ	Equivalence ratio
ρ	Density
ξ_{loss}	Heat loss fraction
A_{21}	Rate of radiative decay
c	Concentration
f_0	Mass burning flux
h_0	Inlet gas enthalpy
I	Chemiluminescence emission intensity
I_s	Specific chemiluminescence emission intensity
k	Thermal conductivity
P	Flame power
q	Heat flux
Q_{21}	Global rate of quenching
S_L	Adiabatic laminar burning velocity
T_0	Reactant stream temperature at burner outlet
T_b	Burnt gas temperature
T_u	Reactant stream temperature before entering the burner
u_0	Mean bulk velocity of reactant stream at burner outlet
V	Diffusion velocity
Y	Mass fraction
y	Fluorescence yield of excited species
exp	Superscript for experimental results
sim	Superscript for simulation results

Acknowledgments

The authors gratefully acknowledge the support of Bosch Thermotechnologie. They also wish to thank David Charalampous for his help with spectrometry and Yannick Le Teno for his help on the design of the experimental setup.

Funding

This work was supported by FUI (Fonds Unique Interministériel).

References

- Alviso, D., Rolon, J., Scouflaire, P., and Darabiha, N. 2015. Experimental and numerical studies of biodiesel combustion mechanisms using a laminar counterflow spray premixed flame. *Fuel*, **153**, 154–165.
- Arias, L., Torres, S., Sbarbaro, D., and Farias, O. 2008. Photodiode based sensor for flame sensing and combustion process monitoring. *Appl Opt.*, **47**(29), 5541–5549. doi:10.1364/AO.47.005541
- Ballester, J., Hernández, R., Sanz, A., Smolarz, A., Barroso, J., and Pina, A. 2009. Chemiluminescence monitoring in premixed flames of natural gas and its blends with hydrogen. *P. Combust. Inst.*, **32**(2), 2983–2991. doi:10.1016/j.proci.2008.07.029
- Barra, A.J., and Ellzey, J.L. 2004. Heat recirculation and heat transfer in porous burners. *Combust. Flame*, **137**(1–2), 230–241. doi:10.1016/j.combustflame.2004.02.007
- Borghi, R., and Champion, M. 2000. *Modélisation et théorie des flammes*, Editions Technip, Paris, ISBN : 2 7108 0758 0 .
- Botha, J.P., and Spalding, D.B. 1954. The laminar flame speed of propane/air mixtures with heat extraction from the flame. *Pro. Roy. Soc. London A*, **225**(1160), 71–96. doi:10.1098/rspa.1954.0188
- Candel, S., Schmitt, T., and Darabiha, N. 2011. Progress in transcritical combustion: experimentation, modeling and simulation. In *Proceedings of 23rd ICDERS*, Irvine USA, pp. 27.
- de Goey, L., van Oijen, J., Kornilov, V., and Ten Thije Boonkkamp, J. 2011. Propagation, dynamics and control of laminar premixed flames. *P. Combust. Inst.*, **33**(1), 863–886. doi:10.1016/j.proci.2010.09.006
- Ding, Y., Durox, D., Darabiha, N., and Schuller, T. 2017. Effect of fuel composition on the flame chemiluminescence. In *Proceedings of the European Combustion Meeting 2017*, Dubrovnik, Croatia, April 18–21.
- Docquier, N., Lacas, F., and Candel, S. 2002. Closed loop equivalence ratio control of premixed combustors using spectrally resolved chemiluminescence measurements. *P. Combust. Inst.*, **29**(1), 139–145. doi:10.1016/S1540 7489(02)80022 0
- Durox, D., Baillet, F., Searby, G., and Boyer, L. 1997. On the shape of flames under strong acoustic forcing: a mean flow controlled by an oscillating flow. *J Fluid Mech*, **350**, 295–310. doi:10.1017/S0022112097006940
- García Armingol, T., and Ballester, J. 2014a. Flame chemiluminescence in premixed combustion of hydrogen enriched fuels. *Int J Hydrogen Energy*, **39**(21), 11299–11307. doi:10.1016/j.ijhydene.2014.05.109
- García Armingol, T., and Ballester, J. 2014b. Influence of fuel composition on chemiluminescence emission in premixed flames of CH₄/CO₂/H₂/CO blends. *Int J Hydrogen Energy*, **39**(35), 20255–20265. doi:10.1016/j.ijhydene.2014.10.039
- Gaydon, A. 1974. *The Spectroscopy of Flames*, Second Edition, Springer.
- Geddis, P.J. (2009). Evaluation of chemiluminescence as a measurement option for industrial flame monitoring and process control. PhD thesis, University of Toronto.
- Guethé, F., Guyot, D., Singla, G., Noiray, N., and Schuermans, B. 2012. Chemiluminescence as diagnostic tool in the development of gas turbines. *Appl. Phys. B*, **107**(3), 619–636. doi:10.1007/s00340 012 4984 y

- Guiberti, T., Durox, D., and Schuller, T. 2017. Flame chemiluminescence from CO₂ and N₂ diluted laminar CH₄/air premixed flames. *Combust. Flame*, **181**, 110–122. doi:10.1016/j.combustflame.2017.01.032
- Guyot, D., Guethe, F., Schuermans, B., Lacarelle, A., and Paschereit, C.O. 2010. CH^{*}/OH^{*} chemiluminescence response of an atmospheric premixed fl under varying operating conditions. GT2010 23135. In *ASME Turbo Expo 2010*, Glasgow, UK, June 10–18.
- Hardalupas, Y., and Orain, M. 2004. Local measurements of the time dependent heat release rate and equivalence ratio using chemiluminescent emission from a flame. *Combust. Flame*, **139**(3), 188–207. doi:10.1016/j.combustflame.2004.08.003
- Hardalupas, Y., Orain, M., Panoutsos, C.S., Taylor, A., Olofsson, J., Seyfried, H., Richter, M., Hult, J., Aldén, M., Hermann, F., and Klingmann, J. 2004. Chemiluminescence sensor for local equivalence ratio of reacting mixtures of fuel and air (FLAMESEEK). *Appl. Therm. Eng.*, **24**(11–12), 1619–1632. Industrial Gas Turbine Technologies doi:10.1016/j.applthermaleng.2003.10.028
- Hardalupas, Y., Panoutsos, C., and Taylor, A. 2010. Spatial resolution of a chemiluminescence sensor for local heat release rate and equivalence ratio measurements in a model gas turbine combustor. *Exp. Fluids*, **49**(4), 883–909. doi:10.1007/s00348-010-0915-z
- Higgins, B., McQuay, M., Lacas, F., and Candel, S. 2001a. An experimental study on the effect of pressure and strain rate on CH chemiluminescence of premixed fuel lean methane/air flames. *Fuel*, **80**(11), 1583–1591. doi:10.1016/S0016-2361(01)00040-0
- Higgins, B., McQuay, M., Lacas, F., Rolon, J. C., Darabiha, N., and Candel, S. 2001b. Systematic measurements of OH chemiluminescence for fuel lean, high pressure, premixed, laminar flames. *Fuel*, **80**(1), 67–74. doi:10.1016/S0016-2361(00)00069-7
- Hurle, I.R., Price, R.B., Sugden, T.M., and Thomas, A. 1968. Sound emission from open turbulent premixed flames. *Pro. Roy. Soc. London A*, **303**(1475), 409–427. doi:10.1098/rspa.1968.0058
- Johnson, M., Kostiuk, L., and Cheng, R. 1998. A ring stabilizer for lean premixed turbulent flames. *Combust. Flame*, **114**(3–4), 594–596. doi:10.1016/S0010-2180(97)00353-2
- Kedia, K.S., and Ghoniem, A.F. 2012. Mechanisms of stabilization and blowoff of a premixed flame downstream of a heat conducting perforated plate. *Combust. Flame*, **159**(3), 1055–1069. doi:10.1016/j.combustflame.2011.10.014
- Kojima, J., Ikeda, Y., and Nakajima, T. 2000. Spatially resolved measurement of OH^{*}, CH^{*}, and C₂^{*} chemiluminescence in the reaction zone of laminar methane/air premixed flames. *P. Combust. Inst.*, **28**(2), 1757–1764. doi:10.1016/S0082-0784(00)80577-9
- Kojima, J., Ikeda, Y., and Nakajima, T. 2005. Basic aspects of OH(A), CH(A), and C₂(d) chemiluminescence in the reaction zone of laminar methane air premixed flames. *Combust. Flame*, **140**(1–2), 34–45. doi:10.1016/j.combustflame.2004.10.002
- Konnov, A.A. (2015). The temperature and pressure dependences of the laminar burning velocity: experiments and modeling. In *Proc. 7th European Combustion Meeting, Budapest, Hungary*, March–April 30–2.
- Lauer, M., and Sattelmayer, T. 2010. On the adequacy of chemiluminescence as a measure for heat release in turbulent flames with mixture gradients. *J. Eng. Gas Turb. Power*, **132**(6), 061502. doi:10.1115/1.4000126
- Lauer, M., Zellhuber, M., Sattelmayer, T., and Aul, C.J. 2011. Determination of the heat release distribution in turbulent flames by a model based correction of OH^{*} chemiluminescence. *J. Eng. Gas Turb. Power*, **133**(12), 121501. doi:10.1115/1.4004124
- Law, C. 1989. Dynamics of stretched flames. *Symp. (Int.) Combust.*, **22**(1), 1381–1402. doi:10.1016/S0082-0784(89)80149-3
- Law, C., and Sung, C. 2000. Structure, aerodynamics, and geometry of premixed flameslets. *Prog. Energy Combust. Sci.*, **26**(4–6), 459–505. doi:10.1016/S0360-1285(00)00018-6
- Lewis, B., and Von Elbe, G. 1987. *Combustion, Flames and Explosions of Gases*, Academic Press, New York, ISBN :978-0-12-446751-4.
- Mazas, A., Fiorina, B., Lacoste, D., and Schuller, T. 2011. Effects of water vapor addition on the laminar burning velocity of oxygen enriched methane flames. *Combust. Flame*, **158**(12), 2428–2440. doi:10.1016/j.combustflame.2011.05.014

- Mejia, D., Selle, L., Bazile, R., and Poinso, T. 2015. Wall temperature effects on flame response to acoustic oscillations. *P. Combust. Inst.*, **35**(3), 3201–3208. doi:10.1016/j.proci.2014.07.015
- Nori, V., and Seitzman, J. (2007). Chemiluminescence measurements and modeling in syngas, methane and jet a fueled combustors. In *45th AIAA Aerospace Sciences Meeting and Exhibit*, Reno, NV, January 8–11.
- Nori, V.N., and Seitzman, J.M. 2009. CH* chemiluminescence modeling for combustion diagnostics. *P. Combust. Inst.*, **32**(1), 895–903. doi:10.1016/j.proci.2008.05.050
- Orain, M., and Hardalupas, Y. 2010. Effect of fuel type on equivalence ratio measurements using chemiluminescence in premixed flames. *C. R. Mecanique*, **338**(5), 241–254. doi:10.1016/j.crme.2010.05.002
- Panoutsos, C., Hardalupas, Y., and Taylor, A. 2009. Numerical evaluation of equivalence ratio measurement using OH* and CH* chemiluminescence in premixed and non premixed methane air flames. *Combust. Flame*, **156**(2), 273–291. doi:10.1016/j.combustflame.2008.11.008
- Samaniego, J. M., Egolfopoulos, F., and Bowman, C. 1995. CO2* chemiluminescence in premixed flames. *Combust. Sci. Technol.*, **109**(1–6), 183–203. doi:10.1080/00102209508951901
- Smith, G.P., Golden, D.M., Frenklach, M., Eiteener, B., Goldenberg, M., Bowman, C.T., Hanson, R. K., Gardiner, W.C., Lissianski, V.V., and Qin, Z.W. 2000. GRI Mech 3.0. http://www.me.berkeley.edu/gri_mech/.
- Smith, G.P., Luque, J., Park, C., Jeffries, J.B., and Crosley, D.R. 2002. Low pressure flame determinations of rate constants for OH(A) and CH(A) chemiluminescence. *Combust. Flame*, **131**(1–2), 59–69. doi:10.1016/S0010-2180(02)00399-1
- Smooke, M.D. 1982. Solution of burner stabilized premixed laminar flames by boundary value methods. *J. Comput. Phys.*, **48**(1), 72–105. doi:10.1016/0021-9991(82)90036-5
- Van Maaren, A., Thung, D., and De Goey, L.R.H. 1994. Measurement of flame temperature and adiabatic burning velocity of methane/air mixtures. *Combust. Sci. Technol.*, **96**(4–6), 327–344. doi:10.1080/00102209408935360
- Zimmer, L., Tachibana, S., Yamamoto, T., Kurosawa, Y., and Suzuki, K. (2003). Evaluation of chemiluminescence as sensor for lean premixed combustion. In *4th Symposium on Smart Control of Turbulence*, Tokyo, Japan, March 2–4.

Appendix A: Gas temperature measurement

Figure 19 is an example of the gas temperature evolution over 30 s at the porous plug burner outlet after the flame blow off. The flow conditions for the burner in operation are $u_0/S_L = 0.29$, $\phi = 1.0$. The delay of the first point corresponds to the time necessary to set the thermocouple in place and is estimated to be (1.5 ± 0.5) s. A regression is then performed assuming an exponential drop according to Newton's cooling law:

$$T - T_e = A \exp(-Bt) \quad (7)$$

where T stands for the gas temperature, T_e the final temperature of the gas and t the time. The positive coefficients A and B as well as T_e are determined by a regression. It is worth noticing that T_e does not correspond to the room temperature (i.e. $\sim 20^\circ\text{C}$). Generally the value T_e given by the regression is slightly below the asymptotic temperature at $t = 30$ s, which may correspond to the supporting plate temperature. An extrapolation to $t = 0$ s yields the gas temperature when the burner is in operation. The time uncertainty of the first point leads to an error of less than 10 K. Tests were also made where the first point of the temperature measurements was left out. It turned out that in most cases, the first measured temperature point that was left out dropped close to the regression curve calculated without considering this first measurement. These tests validate the reliability of the technique used to determine the temperature T_0 with the burner in operation. Repeatability tests have shown that for all cases explored T_0 could be determined in this way with a relative uncertainty of ± 40 K.

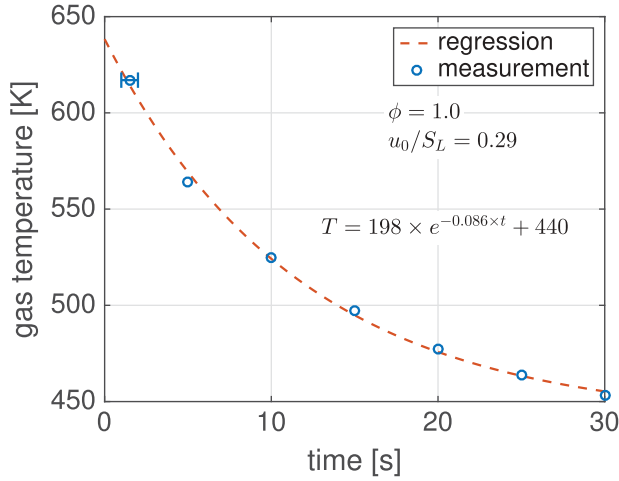


Figure 19. Evolution of the air flow temperature after flame blow off. $u_0/S_L = 0.29$, $\phi = 1.0$.

Appendix B: Results on the multi-perforated burner

The evolution of the specific chemiluminescence intensity with the gas flowrate is also investigated on the cylindrical multi perforated burner. The view angle of observation is perpendicular to the burner axis, and the spectrometer field of view samples a representative circular interrogation area of 30 mm diameter on the burner surface. The results are shown in Figure 20. The gas velocity u_0 is calculated by dividing the gas volumetric flowrate by the sum of the surface areas of all injection holes. Similar to the results found for the porous plug burner in Figure 8, the specific intensity is not constant in Figure 20 in the regime $u_0/S_L < 1$. However, a major difference with results shown in Figure 8 is that for stoichiometric mixtures, the specific intensities of the OH^* and CO_2^* signals do not exhibit a saturation even in the regime $u_0/S_L > 1$. Several factors may be responsible for this behavior:

- It is difficult to determine the exact gas velocity u_0 at the burner outlet due to the nonuniform gas distribution in the wide set of injection holes. Furthermore, the flow expands downstream the small injection holes and occupy the interspace between the holes.
- Another difficulty is that many of the flames are detached at the bottom in the multi perforations of the burner. It is thus difficult to clearly identify the stabilization regime of the flames in these regions and more globally over the entire surface of the burner.
- The flow of burnt gases along the sidewall of the burner is subjected to natural convection. These phenomena are likely to disturb the chemiluminescence characterization.

Nevertheless, the same general features are observed for both the cylindrical multi perforated burner and the porous plug burner. Both setups exhibit large heat transfer to the solid surface and preheating of the reactant stream. In both cases, this leads to a nonlinear evolution of the chemiluminescence intensity signal as the gas flowrate is varied.

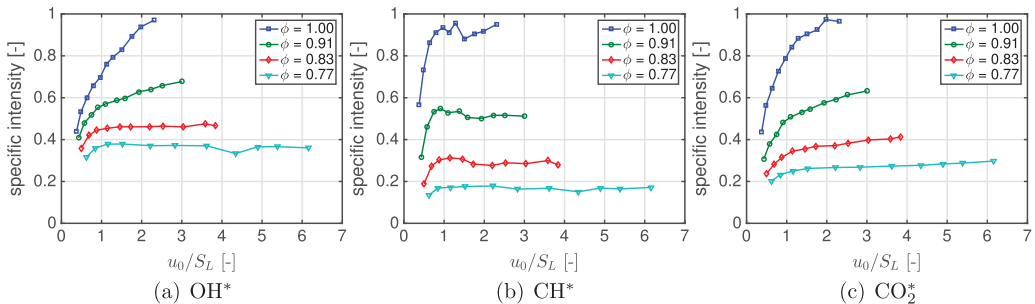


Figure 20. Specific emission intensities I_s^{exp} of OH^* , CH^* and CO_2^* for measurements conducted with the cylindrical multi-perforated burner.